

Cluster Expansion Method for Simulating Realistic Size of Nanoparticle Catalysts with an Application in CO₂ Electroreduction

Taedaehyeong Eom,[†] Won June Kim,[‡] Hyung-Kyu Lim,[§] Myung Hoon Han,^{||} Kyeong Hwan Han,^{||} Eok-Kyun Lee,^{||} Sébastien Lebègue,[‡] Yun Jeong Hwang,[⊥] Byoung Koun Min,[⊥] and Hyungjun Kim^{*,†,||}

[†]Graduate School of EEWS and ^{||}Department of Chemistry, Korea Advanced Institute of Science and Technology (KAIST), Yuseong-gu, Daejeon 34141, Korea

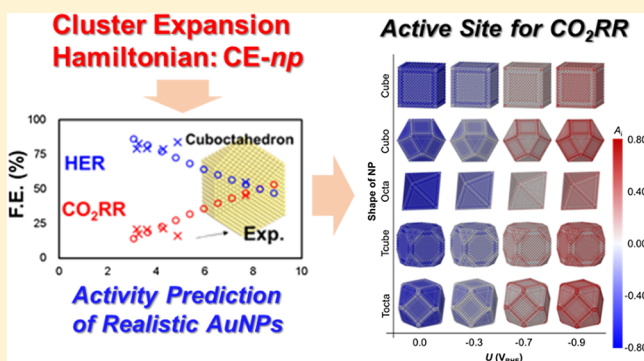
[‡]Université de Lorraine and CNRS, LPCT, UMR 7019, 54506 Vandœuvre-lès-Nancy, France

[§]Department of Chemical Engineering, Kangwon National University, Chuncheon, Gangwon-do 24341, Korea

[⊥]Clean Energy Research Center, Korea Institute of Science and Technology (KIST), Seoul 02792, Korea

Supporting Information

ABSTRACT: For the last several decades, there has been a rapid development of nanoscience and nanotechnology. In particular, nanoparticles (NPs) are applied in various catalyst problems, where their enormously large surface-to-volume ratio not only is advantageous for high catalytic performance but also allows the quantum size effect to play a key role in modifying their chemical properties. However, when understanding the size effect of NPs on the catalytic properties by employing density functional theory (DFT) calculations, there has been an obvious experiment–theory gap in simulating nanocatalysts with realistic sizes. In this study, we developed a new simulation method based on the cluster expansion model, namely, CE-*np*, which enables efficient and accurate calculations of the intermediate binding energies for various sizes of NPs. We then applied CE-*np* to investigate the electrochemical CO₂ reduction reaction (CO₂RR) of gold NPs (AuNPs). CE-*np* reproduces not only DFT-level accuracies in predicting the intermediate binding energies on the NPs and slab surfaces but also the experimental behavior of catalytic activity and selectivity of AuNP catalysts. Because of the high computational efficiency of CE-*np* (without sacrificing the accuracy level of DFT), we performed the most exhaustive search on all possible on-top binding sites of AuNPs to unveil the complicated relations between the catalytic performance (activity and selectivity) and the NP properties (shape and size). This also highlights for the first time the catalytic importance of the near-edge sites, that is, active sites on the facets that are very close to the edges. We anticipate that our methodological development and several new findings on the CO₂RR activity of AuNPs will provide advances in developing CO₂ electrochemical reduction technologies based on NPs.



INTRODUCTION

Over the last several decades, there has been remarkable progress in synthesizing, shape-controlling, and characterizing various metal nanoparticles (NPs).¹ Metal NPs often show unprecedented chemophysical properties that differ from the bulk states of metals, which is due to a strong quantum size effect.^{2,3} This causes metal NPs to exhibit tunable catalytic^{4–6} and optical properties^{7,8} as a function of their size and shape.

Among the various possible applications of metal NPs, NP catalysts have their own impact, which originates from their extremely high surface-to-volume ratio.⁹ By optimizing their size, shape, and compositions, researchers have demonstrated that the performance of nanocatalysts (catalytic activity and selectivity) can be significantly modified. To design and develop new NP catalysts, it is thus required to understand

the detailed interrelation between the NP properties and catalytic performance.

Density functional theory (DFT) calculations have been successfully employed to investigate the complex reaction mechanism of heterogeneous catalysts.¹⁰ Density functional approximation for the exchange–correlation energy enables a reasonably accurate description of the chemical reaction energetics at an acceptable computational cost. Using the current computing power, however, the system size available in routine DFT calculations is still limited to approximately 10² to 10³ atoms. Consequently, for NP systems, where translational symmetry is broken and periodic boundary conditions thus cannot be applied, the practically available size for DFT

Received: March 26, 2018

Published: April 3, 2018

calculations is limited to ca. 2–3 nm (Figure 1). However, such a size regime is near the lower bound of the experiments, and

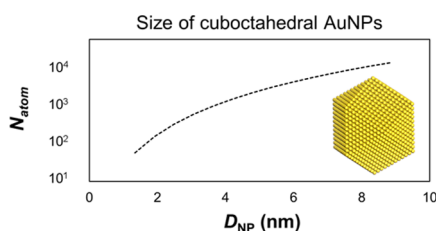


Figure 1. Dramatic increase in the number of atoms (N_{atom}) with an increase in the NP diameter (D_{NP}) limits the direct DFT calculations for the realistic sizes of NPs larger than ca. 3 nm.

the nanocatalyst size often increases to tens of nanometers. Thus, there exists an obvious experiment–theory gap in the length scale.

To bridge such an experiment–theory gap, we here develop an efficient way to calculate the adsorption energies of reaction intermediates on the surface of a nanocatalyst, even for a size of tens of nanometers. As an effective Hamiltonian, we adopt the cluster expansion (CE) method,^{4–6,8,11} which was originally developed to investigate various configurational problems in alloy systems.^{12,13} As the CE model is based on an extended Ising-like model, which is directly related to the lattice gas model, there is a natural relationship between the CE model and surface adsorption problems.^{3,14} Consequently, many previous researchers developed CE models to investigate catalytic problems.^{15–17} Previous CE models mostly construct clusters on the catalyst surface, and thus, their applications have been limited to the case when the catalyst shape and size are fixed to conveniently define the catalyst surface geometry.

In this work, we hence expand the CE model to simulate nanocatalysts with various sizes and different shapes, namely, CE-*np*. This can efficiently estimate adsorption energies at all exposed on-top sites of the nanocatalysts with different particle sizes, which is applied to obtain a comprehensive understanding on the size effect of nanocatalysts for the electrochemical CO₂RR.

THEORETICAL METHODS

Brief Review of the Original CE Method. Within the framework of the CE method, the formation energy of various bulk alloys is expressed as a series of orthogonal cluster correlation functions $\Phi_{\alpha}(\sigma)$, which is constructed by multiplying occupation variables (σ) belonging to the α cluster

$$\begin{aligned} E_f(\sigma) &= \sum_{\alpha} V_{\alpha} \Phi_{\alpha}(\sigma) \\ &= V_0 + \sum_i V_i \sigma_i + \sum_{i,j} V_{ij} \sigma_i \sigma_j + \sum_{i,j,k} V_{ijk} \sigma_i \sigma_j \sigma_k + \dots \end{aligned} \quad (1)$$

where the summation excludes double counting.

For a binary AB alloy, as an example, the occupation variable (σ_i) of a site i is given by either +1 or –1, depending on whether the site is occupied by an A metal or B metal, respectively. Φ_{α} is then defined by the multiplication of σ_i values, consisting of a distinct N-body geometrical framework, that is, a cluster. Consequently, CE can be understood as a generalized Ising-type model.

V_{α} defines the cluster interaction energy, which is usually parameterized against the DFT energies. In particular, as large enough V_{α} values are only meaningful in the summation of eq 2, such V_{α} values are referred to as effective cluster interaction (ECI). The choice of clusters with a significant contribution to $E_f(\sigma)$ is important when constructing the CE model.

Expansion of CE to NP Catalysts: CE-*np*. To describe catalytic problems on the crystalline surface, previous studies have demonstrated that the adsorption energies on the slab surface can be modeled using a two-dimensional CE Hamiltonian.¹⁸ The presence and absence of an adsorbate at site i is here denoted using the occupation variable of $\sigma_i = +1$ and $\sigma_i = -1$, respectively, which successfully captures the adsorption energy variations depending on the adsorbate coverages and configurations.

In our CE model describing the NP catalysts (hereafter referred to as CE-*np*), we define occupation variables in the same manner but simply invert the convention to $\sigma_i = -1$ and $\sigma_i = +1$, respectively, for the presence and absence of an adsorbate. Instead of constructing two-dimensional clusters on the surface, we also consider three-dimensional clusters (as done in the original CE for alloys) and model the energy of the entire system of “NP + adsorbates”. Thereby, a cluster is defined to consist of not only the exposed sites on the NP surface (where σ_i can be either –1 or +1) but also the internal sites inside the NP (where σ_i is always +1 because no adsorbate is allowed).

When an adsorbate is present on the surface site μ , the clusters describing the energy of such a NP are composed of those that include site μ and of others. Then, using eq 1, the total energy of NP with an adsorbate, $E_{\text{NP-ads}}$, can be written as

$$\begin{aligned} E_{\text{NP-ads}}(\sigma) &= \left\{ \sum_{\mu} V_{\mu} \sigma_{\mu} + \sum_{\mu,j} V_{\mu j} \sigma_{\mu} \sigma_j + \sum_{\mu,j,k} V_{\mu j k} \sigma_{\mu} \sigma_j \sigma_k \right. \\ &\quad \left. + \dots \right\} + \left\{ V_0 + \sum_{i \neq \mu} V_i \sigma_i + \sum_{i \neq \mu, j \neq \mu} V_{ij} \sigma_i \sigma_j \right. \\ &\quad \left. + \sum_{i \neq \mu, j \neq \mu, k \neq \mu} V_{ijk} \sigma_i \sigma_j \sigma_k + \dots \right\} \end{aligned} \quad (2)$$

Similarly, we express the energy of the same NP but without an adsorbate at the surface site μ , by employing different occupation variables of $\tilde{\sigma}$, and we bisect the entire cluster summation into one for clusters that included site μ and one for the others

$$\begin{aligned} E_{\text{NP}}(\tilde{\sigma}) &= \left\{ \sum_{\mu} V_{\mu} \tilde{\sigma}_{\mu} + \sum_{\mu,j} V_{\mu j} \tilde{\sigma}_{\mu} \tilde{\sigma}_j + \sum_{\mu,j,k} V_{\mu j k} \tilde{\sigma}_{\mu} \tilde{\sigma}_j \tilde{\sigma}_k \right. \\ &\quad \left. + \dots \right\} + \left\{ V_0 + \sum_{i \neq \mu} V_i \sigma_i + \sum_{i \neq \mu, j \neq \mu} V_{ij} \tilde{\sigma}_i \tilde{\sigma}_j \right. \\ &\quad \left. + \sum_{i \neq \mu, j \neq \mu, k \neq \mu} V_{ijk} \tilde{\sigma}_i \tilde{\sigma}_j \tilde{\sigma}_k + \dots \right\} \end{aligned} \quad (3)$$

Using eqs 2 and 3, we now define the adsorption energy of E_{ads} simply by subtracting eq 3 and the reference energy of the free adsorbate, E_{ads}^0 , from eq 2. It is noted that all of the occupation variables should remain unchanged with or without

an adsorbate, except for the occupation variable at the adsorption site μ ; $\sigma_i = \tilde{\sigma}_i$ for $i \neq \mu$ while $\sigma_\mu = -\tilde{\sigma}_\mu = -1$. Thus, the second parenthesized terms of the right-hand side of eqs 2 and 3 are the same, yielding a simple expression of E_{ads} as follows:

$$\begin{aligned} E_{\text{ads}}(\boldsymbol{\sigma}) &= E_{\text{NP-ads}}(\boldsymbol{\sigma}) - E_{\text{NP}}(\tilde{\boldsymbol{\sigma}}) - E_{\text{ads}}^0 \\ &= V'_0 + \sum_{\mu} V'_{\mu} \tilde{\sigma}_{\mu} + \sum_{\mu j} V'_{\mu j} \tilde{\sigma}_{\mu} \tilde{\sigma}_j + \sum_{\mu j k} V'_{\mu j k} \tilde{\sigma}_{\mu} \tilde{\sigma}_j \tilde{\sigma}_k \\ &\quad + \dots \end{aligned} \quad (4)$$

where the primed values are defined as $V'_0 = -E_{\text{ads}}^0$, $V'_{\mu} = 2V_{\mu}$, $V'_{\mu j} = 2V_{\mu j}$ and $V'_{\mu j k} = 2V_{\mu j k}$. Equation 4 shows that the adsorption energy at the site μ of the NP can be described using the conventional CE formalism but restricting the summation range to only the clusters that include site μ . We refer this subset of the clusters as “reduced clusters”, as illustrated in Figure 2.

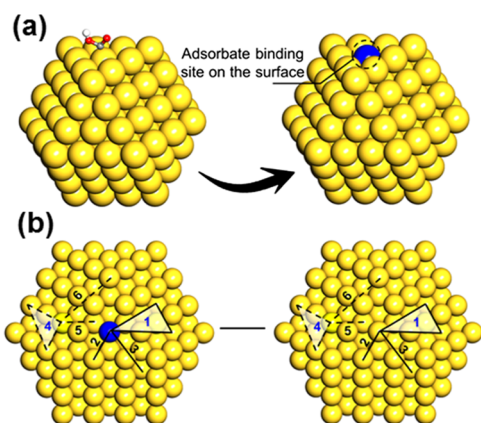


Figure 2. (a) Using the CE model, the absence and presence of adsorbate can be distinguished using different occupation variable of σ_i ; $\sigma_i = -1$ (yellow) and $\sigma_i = +1$ (blue), respectively. (b) Adsorbate binding energy is expressed as the difference between the energy of “NP with an adsorbate” (left) and the energy of “NP without an adsorbate” (right). During this subtraction, the energy contribution from the clusters without the adsorption site included (e.g., 4, 5, 6) vanishes, and thus, the binding energy is expanded using only the clusters with the adsorption site included (e.g., 1, 2, 3)—“reduced clusters”.

However, because of the loss of translational symmetry of the lattice, many sites in the NP system become nonequivalent compared with the bulk system. Previously, to investigate the configurational thermodynamics of alloyed NPs,¹¹ Wang et al. suggested distinguishing nonequivalent clusters based on the point group symmetry of NP. Similarly, a strategy to construct a layer-wise CE was also suggested to study alloy surfaces.¹⁹

In our CE-*np*, we distinguish only the two-body clusters by differentiating the undercoordinated surface sites from the fully coordinated internal sites of the NP. A cluster consisting of “1 surface site + 1 internal site” is distinguished from a cluster consisting of 2 surface sites, even though they have the same interdistance (Figure 3). Compared with the previous method based on point group symmetry, our method leads to far fewer classifications of nonequivalent clusters for the same size of the NP. This is a practical choice to reduce the number of fitting parameters in the CE model Hamiltonian with distinguishing various sizes of NPs using a single form of model Hamiltonian in a convenient manner.

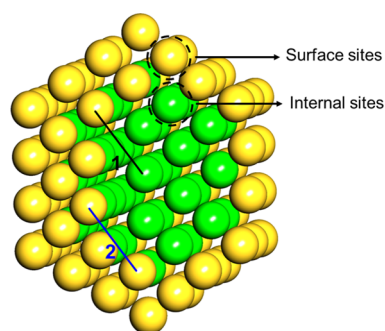


Figure 3. Depending on the sites that construct the cluster either from surface sites (yellow) or internal sites (green), the clusters become inequivalent, even when they have the same shape. In our CE-*np*, the two-body clusters consisting of “1 surface site + 1 internal site” (black; 1) are treated differently than the two-body clusters consisting of “2 surface sites” (blue; 2). This effectively accounts for the effect of the loss of lattice translational symmetry in NPs.

We note that our CE-*np* method can efficiently describe the adsorbate binding energies to various sizes and shapes of NPs but is limited to describe the binding energies only at the low-coverage limit.

ECI Selection. To construct the CE Hamiltonian in practice, we need to parameterize the energetics of the system using a truncated set of ECIs. However, in general, it is not even known how many ECIs should be kept in the CE Hamiltonian,²⁰ thus indicating the difficulty of the ECI selection problem.

To find an optimal and reliable set of ECIs preventing both underfitting and overfitting, we here employed the genetic algorithm (GA) and minimized the cross-validation (CV) error^{21,22}

$$CV^2 = \frac{1}{N_t} \sum_{i=1}^{N_t} (E_{\text{ref}}^i - E_{\text{CE}}^{(i)})^2 \quad (5)$$

where E_{ref}^i is the reference energy of the training set (usually DFT energy) and $E_{\text{CE}}^{(i)}$ is the predicted value using CE fitted against the $N_t - 1$ training set values where E_{ref}^i is excluded (where N_t is the total number of entities in the training set).

During our GA operations, as suggested in a previous study,²³ each “gene” consists of 1’s and 0’s that indicate which ECIs will be included in the energy expression; thus, each gene represents a particular candidate CE model by a string. We first randomly initiate N_p^2 number of genes, which is called an “initial gene pool”. Among the initial gene pool, we select N_p parents’ genes with the highest CV scores (referred as a “dominant gene pool”) and generate N_p^2 children’s genes by crossover and mutating the parents’ genes. To increase the diversity of the new population, we randomly select M_p parents’ genes from the “initial gene pool”, namely, a “randomly selected gene pool”; one parent from the “randomly selected gene pool”, and the other parent from the “dominant gene pool” breed another $N_p \times M_p$ children’s genes. Then, among the total $N_p(N_p + M_p)$ number of children’s genes, we select N_p next-generation parents’ genes with the highest CV scores to breed the following generation. Details of the GA and genetic operations of the crossover and mutation are shown in Figure 4.

DFT Calculations for Training Sets. To prepare the training set energies E_{ref}^i in eq 5, we performed DFT calculations as implemented in the SIESTA code.^{24,25} To

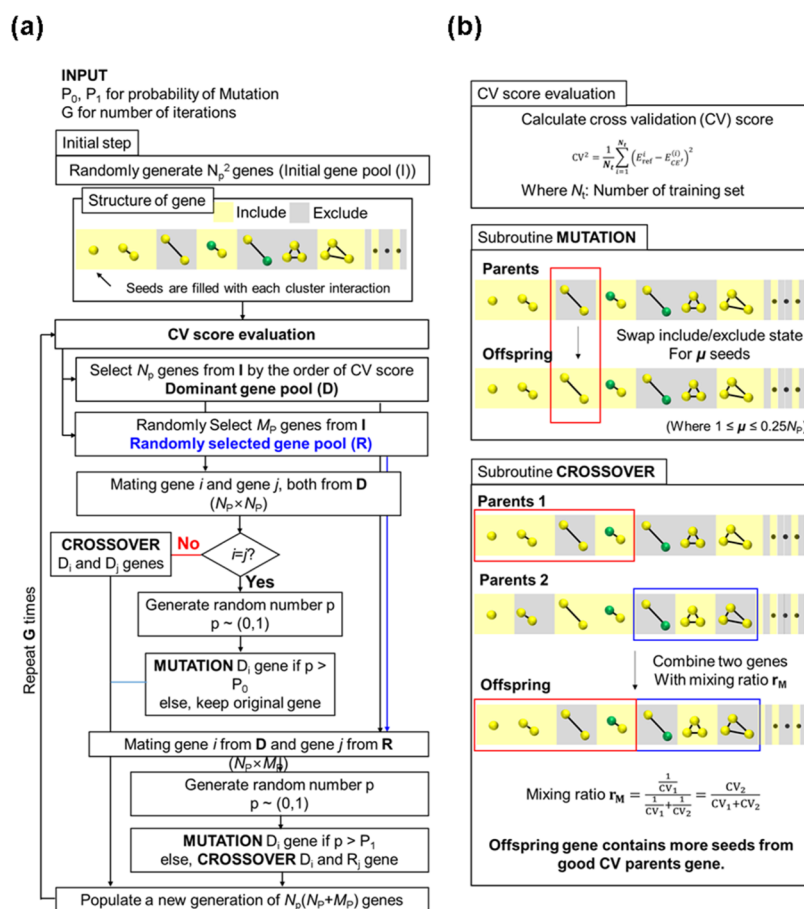


Figure 4. (a) Flowchart showing the details of GA utilized to select ECIs. (b) Details of the CV score evaluation and genetic operations (mutation and crossover).

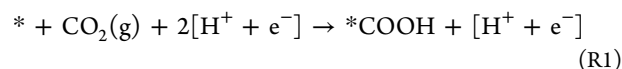
describe the exchange–correlation functional, we used the generalized-gradient approximation by Perdew, Burke, and Ernzerhof (PBE)²⁶ and the numerical atomic orbitals²⁷ as the basis functions describing the valence electrons. The interactions between the valence electrons and the core electrons were treated using norm-conserving pseudopotentials, including nonlinear partial-core corrections.²⁸ We set an energy cutoff value of 250 Ry, and all structures were fully optimized (in the presence and absence of the adsorbate) until the atomic forces converged to less than 0.01 eV/Å.

RESULTS AND DISCUSSION

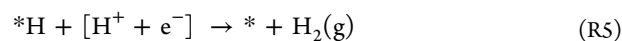
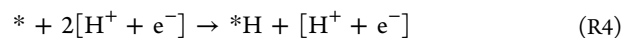
CO₂ Electrochemical Reduction Reaction (CO₂RR) Versus Hydrogen Evolution Reaction (HER). Using our CE-*np* model described above, we now investigate the CO₂-to-CO electrochemical reduction, CO₂RR, of gold NP (AuNP) catalysts. To mitigate the anthropogenic climate change, developing technologies to convert CO₂ into other useful chemical forms is considered one of the most urgent challenges.^{29–33} Unlike other catalytic problems, where nanostructuring is usually advantageous for increasing the catalytic activity because of the substantial increase in the surface-to-volume ratio, previous experiments have shown that nanosizing the CO₂RR nanocatalysts is complicatedly related to the catalytic performance:³⁴ sometimes it increases the activity,¹³ sometimes it significantly degrades the selectivity by significantly increasing the activity of the hydrogen evolution reaction (HER),^{35,36} and sometimes it substantially alters the product

distribution.³⁷ To develop a comprehensive understanding of the size effect of nanocatalysts on the electrochemical CO₂RR, we here apply our CE-*np* method, which allows exhaustive investigations of all possible on-top binding sites of nanocatalysts with a wide range of particle shapes and sizes.

From previous studies, it is widely known that CO₂RR to CO occurs via the following three elementary steps.^{38–40} Thus, it is important to model the adsorption energies of COOH and CO to the catalyst surface.



However, the HER via proton reduction is competitive with CO₂RR, which deteriorates the product selectivity. The reactivity of the HER is usually calculated using the Volmer–Heyrovsky type of reaction pathway, where the adsorption energy of H is important



As a training set, we thus calculated the adsorption energies of COOH, CO, and H on AuNP using DFT. We denote the binding energies at the surface site i as $\Delta E_{b@i}^{\text{COOH}}$, $\Delta E_{b@i}^{\text{CO}}$ and $\Delta E_{b@i}^{\text{H}}$, respectively, where *COOH, CO, and 1/2H₂ are used as

reference states of free adsorbates. Because of the practical convenience of constructing clusters only using the lattice sites of NP, we restrict our discussion to the binding energies for the case of an adsorbate in an on-top position. This approximation may bring an artifact in describing the H binding because it is known to adsorb to the hollow or bridge sites.^{17,41} However, we note that the COOH and CO are known to mostly bind to the on-top site. As such, we conceive that the CO₂RR, which is the major focus of this work, can be reasonably described using our CE-*np* method, and the relative activity and/or trend of the HER can also be reasonably captured.

In the training set, we included three different shapes of fcc-packed AuNPs, (i) octahedron, (ii) cube, and (iii) cuboctahedron (Figure 5a–c), with sizes varying from 32 to 309 atoms

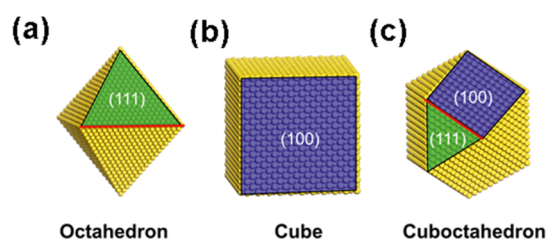


Figure 5. Three different shapes of AuNPs considered to generate training sets: (a) octahedron consisting of (111) facets, (b) cube consisting of (100) facets, and (c) cuboctahedron consisting of (111) and (100) facets.

(corresponding to the range from ~ 1.1 to ~ 2.4 nm). In detail, we employed four different sizes of octahedral AuNPs (# of atoms = 44, 85, 146, 231), three different sizes of cuboctahedral AuNPs (# of atoms = 55, 147, 309), and five different sizes of cubic AuNPs (# of atoms = 32, 63, 108, 172, 256) as shown in Figures S1–S3.

At the external surface of each NP with a certain size, there exists a number of symmetrically inequivalent adsorption sites, all of which are under the DFT investigations of adsorption energies. In total, we calculated 186 different binding energies of COOH, CO, and H on various shapes and sizes of AuNP, all of which are listed in Tables S1 and S2. We also show the representative DFT optimized structures of AuNPs with an adsorbate in Figures S4–S6.

Construction and Validation of CE Hamiltonian. We construct the CE Hamiltonian by considering up to 16th nearest-neighbor pairs and triplets and minimize the CV error using GA. The change of CV error over the course of the optimization process is shown in Figure S7. The selected ECIs using GA consist of 3 doublets and 19 triplets to describe the COOH binding energies, 7 doublets and 10 triplets to describe the CO binding energies, and 2 doublets and 16 triplets to describe the H binding energies (Figures 6a and S8–S10).

The binding energies predicted using the optimized CE-*np* method, $\Delta E_{b(\text{CE-}np)}$, are compared with the reference binding energies from DFT, $\Delta E_{b(\text{DFT})}$, in Figure 6b. For COOH and CO, we find that CE-*np* predicts the binding energy with a nearly perfect accuracy ($\Delta E_{b(\text{DFT})}^{\text{COOH}} = 1.0000 \times \Delta E_{b(\text{CE-}np)}^{\text{COOH}}$ with $R^2 = 0.94$ and $\Delta E_{b(\text{DFT})}^{\text{CO}} = 1.0000 \times \Delta E_{b(\text{CE-}np)}^{\text{CO}}$ with $R^2 = 0.94$). However, CE-*np* slightly underestimates the H binding energy, although the error is still within an acceptable range ($\Delta E_{b(\text{DFT})}^{\text{H}} = 1.0361 \times \Delta E_{b(\text{CE-}np)}^{\text{H}}$ with $R^2 = 0.85$).

To assess the critical importance of the CE-*np* method in predicting binding energies, we show the change in binding energies with respect to the coordination number (CN) or the

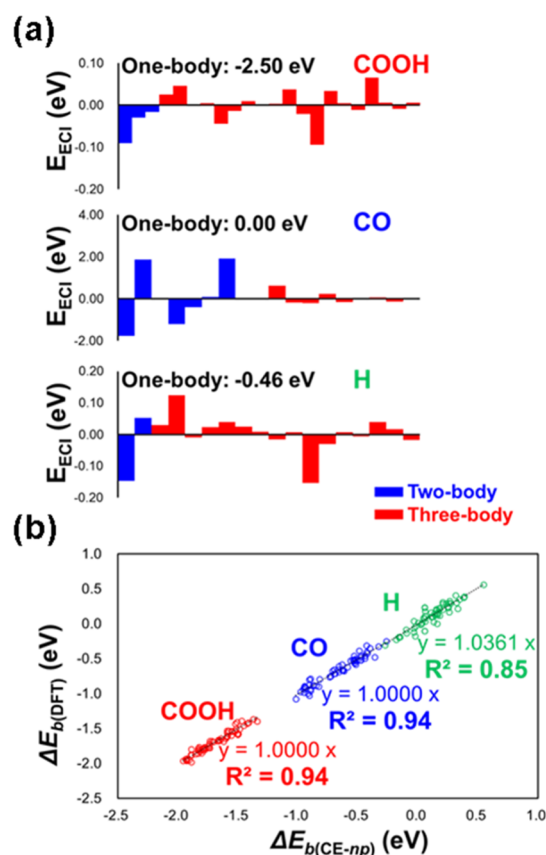


Figure 6. (a) Selected ECIs for describing COOH, CO, and H binding energies, and (b) correlation between the predicted binding energies using CE-*np*, $\Delta E_{b(\text{CE-}np)}$, vs DFT binding energies, $\Delta E_{b(\text{DFT})}$, for COOH (red), CO (blue), and H (green).

generalized CN in Figure S11. It clearly shows that a rather simple idea, that is, assuming that a less-coordinated site would have a stronger binding, is quantitatively erroneous in this case, demonstrating R^2 values of ~ 0.7 for COOH and CO bindings and < 0.1 for H bindings. This is presumably ascribed to the complicated NP–adsorbate interaction, where the covalent and metallic characters are coexisting.⁴²

To further validate our CE-*np* model, we examine the change in predicted binding energies at the center of facets with increasing AuNP sizes (Figure 7). We find that the COOH (or CO) binding energy from CE-*np* converges to -1.67 (or -0.51) eV at the center of the (111) facets of octahedral and cuboctahedral NPs, which is compared with the DFT binding energy of -1.60 (or -0.44) eV calculated using the Au(111) slab model with 1/16 monolayer (ML) coverage (Figure 7a). Similarly, the COOH (or CO) binding energy from CE-*np* converges to -1.80 (or -0.75) eV at the center of the (100) facets of cubic and cuboctahedral NPs, which is compared with the DFT binding energy of -1.70 (or -0.72) eV calculated using Au(100) slab model with 1/18 ML (Figure 7b). For the case of H, the binding energies converge into 0.26 eV for the (100) facet and 0.21 eV for the (111) facet of AuNP, which are comparable with the values of 0.26 and 0.18 eV from the (100) and (111) slab models, respectively.

We then investigate the change of predicted binding energies at the middle of the edges with increasing size of AuNPs (Figure 7c). We find a converging behavior of $\Delta E_{b(\text{CE-}np)}^{\text{COOH}}$, $\Delta E_{b(\text{CE-}np)}^{\text{CO}}$, and $\Delta E_{b(\text{CE-}np)}^{\text{H}}$ to $-1.74/-1.80/-1.81$ eV, $-0.68/-$

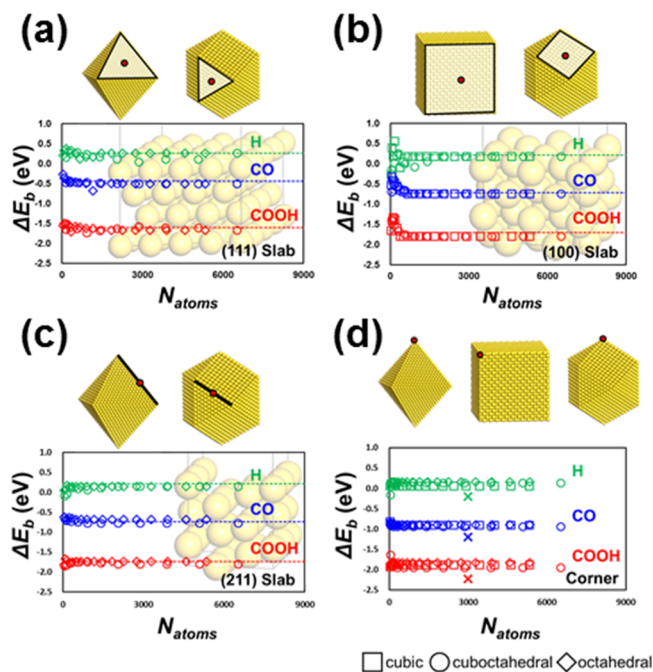


Figure 7. Changing of binding energies calculated using CE-*np*, $\Delta E_{b(\text{CE-}np)}$ at the high-symmetric sites of AuNP with an increasing number of atoms in the NPs (N_{atoms}), that is, NP size; (a) binding at the center of (111) facets of octahedral and cuboctahedral AuNPs, (b) binding at the center of (100) facets of cubic and cuboctahedral AuNPs, (c) binding at the middle of the edges of octahedral and cuboctahedral AuNPs, and (d) binding at the corner of octahedral, cubic and cuboctahedral AuNPs. For comparison, DFT calculated binding energies using (111), (100), and (211) slab models are shown as dotted lines in (a–c), respectively. For the comparison of binding energies at corner sites, DFT calculated binding energies using Au₁₃ cluster are shown using cross marks (×).

0.87/−0.78 eV, and 0.14/0.19/0.14 eV, respectively, for the edge of octahedral/cubic/cuboctahedral NPs. These are comparable to the values calculated at the edge of the stepped surface of the (211) slab, which are −1.74 eV for COOH binding, −0.74 eV for CO binding, and 0.21 eV for H binding. This validates the previous theoretical attempt, which tries to model the binding energy at the edge of the AuNP using a stepped surface.¹³

In addition, we investigate the binding energy change at the corner site of NPs with increasing size in Figure 7d. We find a converging behavior of $\Delta E_{b(\text{CE-}np)}^{\text{COOH}}$, $\Delta E_{b(\text{CE-}np)}^{\text{CO}}$, and $\Delta E_{b(\text{CE-}np)}^{\text{H}}$ to −1.83/−1.89/−1.96 eV, −0.90/−0.90/−0.95 eV, and 0.16/0.06/0.13 eV, respectively, for the corner site of octahedral/cubic/cuboctahedral NPs. We find that the Au₁₃ cluster model, which predicts $\Delta E_{b(\text{CE-}np)}^{\text{COOH}}$, $\Delta E_{b(\text{CE-}np)}^{\text{CO}}$, and $\Delta E_{b(\text{CE-}np)}^{\text{H}}$ of −2.22, −1.20, and −0.20 eV, respectively, shows a strongly over-binding tendency, implying that the previous theoretical attempt to model the corner site using Au₁₃ cluster¹³ is erroneous because of a strong finite-size effect.

Catalytic Activities of AuNPs. With the predicted $\Delta E_{b(\text{CE-}np)}^{\text{COOH}}$, $\Delta E_{b(\text{CE-}np)}^{\text{CO}}$, and $\Delta E_{b(\text{CE-}np)}^{\text{H}}$ values from the CE-*np* model in hand, we model the site-specific catalytic activities of different shapes and sizes of AuNP as a function of the external bias potential of U . Using the previously established strong linear correlation between binding energies (ΔE_b) and binding free energies (ΔG_b)^{42,43} for adsorbate binding cases to the metal surfaces, which are shown in Figure S12, we can easily calculate

ΔG_b^{COOH} , ΔG_b^{CO} , and ΔG_b^{H} . Additionally, from the previous study using the computational hydrogen electrode method,⁴⁴ we have formulated the relationship between the binding free energies and the reaction free energies of the CO₂RR elementary steps of R1, R2, and R3 at the active site i ; $\Delta G_i^{\text{R1}}(U) = 2.02 + eU + \Delta G_{b@i}^{\text{COOH}}$, $\Delta G_i^{\text{R2}}(U) = -1.07 + eU + \Delta G_{b@i}^{\text{CO}} - \Delta G_{b@i}^{\text{COOH}}$, and $\Delta G_i^{\text{R3}}(U) = -0.50 - \Delta G_{b@i}^{\text{CO}}$, respectively (Figure S13). It is noted that the external bias potential is defined versus the reversible hydrogen electrode (RHE). Similarly, we calculate the reaction free energies of the elementary steps of the HER by following the procedure established in our previous work,⁴³ $\Delta G_i^{\text{R4}}(U) = eU + (\Delta G_{b@i}^{\text{H}} + 0.23)$ and $\Delta G_i^{\text{R5}}(U) = eU - (\Delta G_{b@i}^{\text{H}} + 0.23)$, where the constant shift of 0.23 eV is introduced to mitigate the overbinding tendency of the PBE functional⁴³ (Figure S14).

We then define the thermodynamic barrier as the reaction energy of the largely disfavored elementary step:

$$\Delta G_i^{\text{CO}_2\text{RR}}(U) = \max\{\Delta G_i^{\text{R1}}(U), \Delta G_i^{\text{R2}}(U), \Delta G_i^{\text{R3}}(U)\} \quad (6)$$

$$\Delta G_i^{\text{HER}}(U) = \max\{\Delta G_i^{\text{R4}}(U), \Delta G_i^{\text{R5}}(U)\} \quad (7)$$

which provides a measure of catalytic activity at the site i ; $A_i = -\Delta G_i(U)$. Then, the overall catalytic activity of the NP, that is, current density, can be formulated as⁴⁵

$$j^{\text{CO}_2\text{RR}}(U) = \frac{1}{S} j_0^{\text{CO}_2\text{RR}} \sum_{i=1}^{N_{\text{surf}}} \exp[-\beta \Delta G_i^{\text{CO}_2\text{RR}}(U)] \quad (8)$$

$$j^{\text{HER}}(U) = \frac{1}{S} j_0^{\text{HER}} \sum_{i=1}^{N_{\text{surf}}} \exp[-\beta \Delta G_i^{\text{HER}}(U)] \quad (9)$$

where $\beta = 1/k_B T$ and N_{surf} is the number of surface atoms exposed on the NP. The prefactors of $j_0^{\text{CO}_2\text{RR}}$ and j_0^{HER} contain all complicated details, including the reaction conditions, such as the local concentration of the reactant/product at the reaction plane and pH; thus, they will be considered system- and condition-dependent variables.

We also simply assumed that the surface area (S) is proportional to the number of exposed atoms at the surface (N_{surf}) with a proportional coefficient of σ ; that is, $S = \sigma N_{\text{surf}}$. We thus rewrite eqs 8 and 9 as

$$j^{\text{CO}_2\text{RR}}(U) = \frac{1}{N_{\text{surf}}} j_0^{\text{CO}_2\text{RR}} \sum_{i=1}^{N_{\text{surf}}} \exp[-\beta \Delta G_i^{\text{CO}_2\text{RR}}(U)] \quad (10)$$

$$j^{\text{HER}}(U) = \frac{1}{N_{\text{surf}}} j_0^{\text{HER}} \sum_{i=1}^{N_{\text{surf}}} \exp[-\beta \Delta G_i^{\text{HER}}(U)] \quad (11)$$

where $j_0^{\text{CO}_2\text{RR}} = j_0^{\text{CO}_2\text{RR}}/\sigma$ and $j_0^{\text{HER}} = j_0^{\text{HER}}/\sigma$. We further define the total current density, $j^{\text{tot}}(U) \equiv j^{\text{CO}_2\text{RR}}(U) + j^{\text{HER}}(U)$, and the Faradaic efficiency (F.E.) of CO₂RR, $\text{F.E.}(U) \equiv j^{\text{CO}_2\text{RR}}(U)/j^{\text{tot}}(U)$.

In this study, we determine the prefactors of $j_0^{\text{CO}_2\text{RR}}$ and j_0^{HER} to reproduce the experimental $j^{\text{tot}}(U)$ and $\text{F.E.}(U)$ of the previous experimental data by Mistry et al.⁵⁵ as shown in Figure S15. Here, the spherical AuNPs in the experiments are considered as octahedral AuNPs. This leads to $j_0^{\text{CO}_2\text{RR}} = 120 \text{ mA/cm}^2$ and $j_0^{\text{HER}} = 2.4 \times 10^{-15} \text{ mA/cm}^2$.

Simulated Linear Sweep Voltammetry and Active Centers. Using eqs 10 and 11, we calculated the voltage-dependent current density for CO₂RR and HER in Figure 8a,b. Using CE-*np*, we investigate five different shapes of fcc-packed NPs: octahedron, truncated octahedron, cube, truncated cube, and cuboctahedron (Figure 8c).

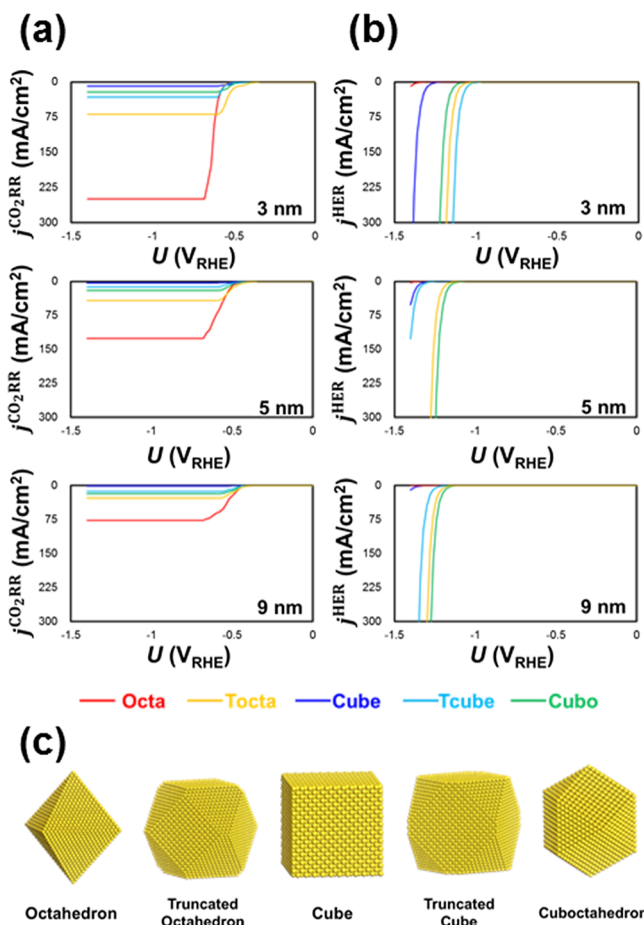


Figure 8. Simulated linear sweep voltammetry for the partial current densities of (a) CO₂RR and (b) HER for 3, 5, and 9 nm sized AuNPs with various shapes. Five different shapes of fcc-packed AuNPs are considered, which are octahedron (Octa; red), truncated octahedron (Tocta; yellow), cube (Cube; blue), truncated cube (Tcube; cyan), and cuboctahedron (Cubo; green) as shown in (c).

For CO₂RR, as shown in Figure 8a, we find that the shape dependency on the on-set potentials is rather marginal but that the maximum current is strongly dependent on the shape that follows the order of octahedron > truncated octahedron > cuboctahedron > cube > truncated cube. Here, it should be noted that only the kinetic current is taken into consideration in our model. Thus, the limited maximum current under high overpotential regime in Figure 8a is not because of the diffusion limit but because of the non-Faradaic CO desorption step; the energetics of CO desorption step is independent on the bias potential while the other Faradaic steps become substantial downhill under high overpotential. By increasing the NP size, we find that the on-set potential decreases from -0.55 V_{RHE} for 3 nm NPs to -0.45 V_{RHE} for 9 nm on octahedral NPs. More detailed analyses of the size dependency are discussed below.

For the HER, as shown in Figure 8b, we find that the on-set potentials are largely dependent on the shape of NPs and that

an exponential increase of the kinetic current density is obtained upon the increase of overpotential because of the lack of non-Faradaic step during the HER. We find that the on-set potential of the truncated cube is the smallest, followed by the order of truncated octahedron, cuboctahedron, cube, and octahedron for 3 nm AuNP, whereas this order is changed to cuboctahedron < truncated octahedron < truncated cube < cube < octahedron for larger sizes.

Active Centers: Importance of Near-Edge Sites. To investigate the location of the active site, we color each surface site of NPs depending on the site-dependent catalytic activity of A_i in Figures 9 and 10. For CO₂RR, as shown in Figure 9, we

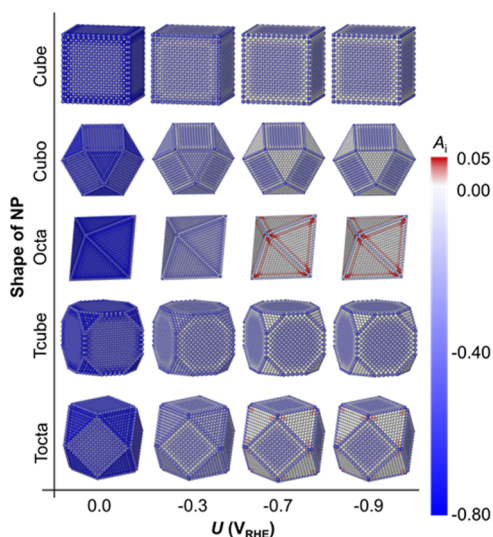


Figure 9. Colormaps showing the site-dependent catalytic activities (A_i) of CO₂RR for five different shapes of AuNPs. Here, AuNPs with the size of 9 nm are representatively shown. The higher value of A_i means the higher catalytic activity at the considered active site, i .

find that the facets are mostly active; in particular, the (111) facet shows a higher activity than does the (100) facet. This

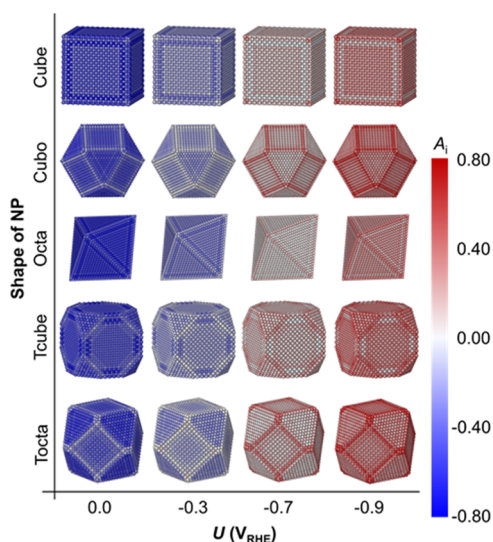


Figure 10. Colormaps showing the site-dependent catalytic activities (A_i) of the HER for five different shapes of AuNPs. Here, AuNPs with the size of 9 nm are representatively shown. The higher value of A_i means the higher catalytic activity at the considered active site, i .

explains the aforementioned shape-dependent activity trend: an octahedron consisting of only (111) facets shows the largest activity, whereas a cube consisting of only (100) facets shows the smallest activity. Truncated octahedron, truncated cube, and cuboctahedron, all of which consist both (111) and (100) facets, show intermediate activity, and their relative activity is correlated with the ratio of exposed (111) facets to (100) facets, as shown in Figure S16. This is different from the previous theoretical discussions claiming the edge and corner of AuNP as the CO₂RR active sites, where the high-symmetric binding sites of the NP surface were only considered.^{13,46,47}

Furthermore, it is more interesting to note that the facet sites close to the edges are more active than are the sites at the middle of the facet, which can be described as near-edge sites. This shows the importance of a finite-size effect and shape dependency in identifying the catalytic active site of NP, which have not been properly examined in previous studies because of large computational costs.

As shown in Figure 10, we further find that the (100) facet sites close to the edge consisting of (100) and (111) facets (which are also a certain type of near-edge sites) are particularly active for the HER. Such near-edge sites are formed in cuboctahedral, truncated cube, and truncated octahedral NPs, which show the largest HER activities in Figure 8. This suggests that minimizing the simultaneous exposure of (100) and (111) facets is important for suppressing the HER.

Size-Dependent Catalytic Activity and F.E. Figure 11a,b shows the change of the current density j as a function of NP size under the bias potential of $U = -1.2$ V_{RHE} for CO₂RR and HER. Overall, we observe that the octahedral and truncated octahedral NPs are highly active for CO₂RR (due to the large exposure of (111) facets) but that the cuboctahedral and

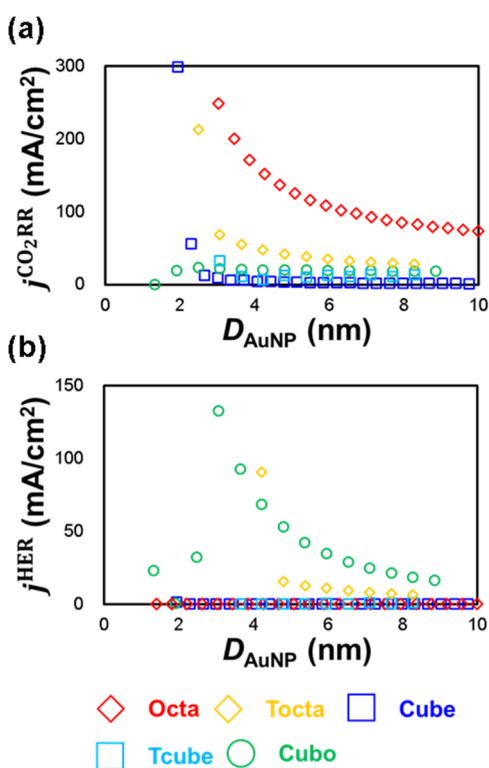


Figure 11. Change of the current densities, j , of (a) CO₂RR and (b) HER as a function of NP size (D_{AuNP}) for five different shapes of AuNPs.

truncated octahedral NPs are highly active for the HER (due to the large exposure of near-edge sites between (100) and (111) facets). When varying the NP size, both the CO₂RR and HER activities show a monotonic decaying tendency after the particle size becomes larger than a certain critical size because of the decrease of the surface-to-volume ratio.

In Figure 12, we show the calculated F.E. We first note that the calculated F.E. of cuboctahedral NPs shows good

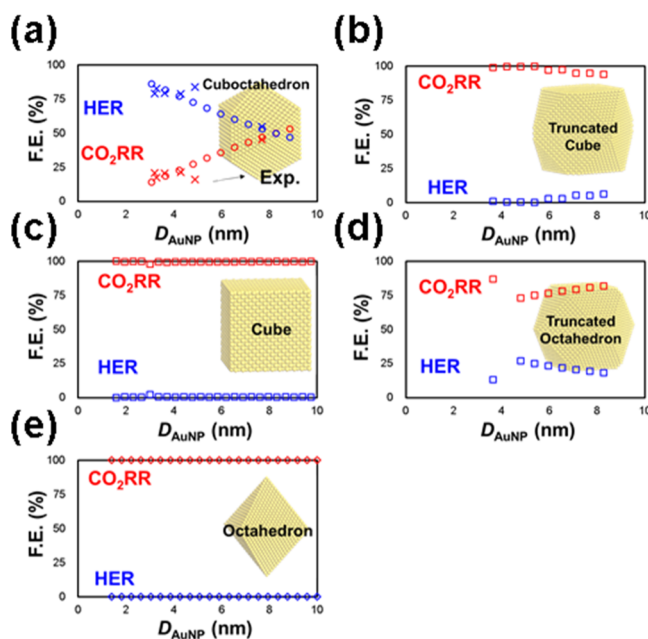


Figure 12. Change of the Faradaic efficiencies, F.E., of CO₂RR (red) and HER (blue) as a function of NP size (D_{AuNP}) for five different shapes of AuNPs: (a) cuboctahedron, (b) truncated cube, (c) cube, (d) truncated octahedron, and (e) octahedron. For comparison, experimental values are shown as cross marks (x) in (a), which are obtained from ref 35.

agreement with the previous experiment by Mistry et al.³⁵ as shown in Figure 12a, because we derived the prefactors of $j_0^{\text{CO}_2\text{RR}}$ and j_0^{HER} in our model from the same experimental data. We also find that the cubic and octahedral NPs show a nearly perfect selectivity toward CO₂RR as shown in Figure 12c,e regardless of the NP size, because of the absence of the simultaneous exposure of (100) and (111) facets, while the truncated octahedral NPs show a limited CO₂RR F.E. of ~75%. We further find that the truncated cubic NPs also show a large enough F.E. for CO₂RR.

Overall, we conclude that the octahedral NPs are superior in CO₂RR, which show the largest partial current density of $j^{\text{CO}_2\text{RR}}$ with high selectivity. In terms of maximizing the activity, our CE-*np* model suggests the use of 2–4 nm octahedral NPs (see Figure 11). However, if one considers a possible deformation path of octahedral NP into truncated octahedral NP by displacing highly undercoordinated corner atoms, it would be more desirable to use ~5 nm octahedral NPs, which would allow the high selectivity to be retained, even after deformation.

CONCLUSIONS

In summary, we developed a CE method for predicting the adsorbate binding energies to the NP surface: CE-*np*. By introducing two important concepts of (1) summation over the

“reduced clusters” and (2) simple treatment of nonequivalent sites by bisecting the sites into surface and internal sites, the adsorbate binding energies from DFT calculations were successfully modeled using a CE-type Hamiltonian.

We then applied our CE-*np* method to investigate the CO₂ electrochemical reduction reaction of AuNPs. On the basis of the accurate and efficient description of adsorbate binding energies of CE-*np*, we simulated voltage-dependent current densities for five different shapes of fcc-packed AuNPs (octahedron, truncated octahedron, cube, truncated cube, and cuboctahedron) with sizes ranging from 2 to 10 nm. By exploring the site-dependent activity at all exposed on-top binding sites for different shapes and sizes of AuNPs, which is practically unavailable for DFT calculations, our simulation results elucidated the catalytic importance of near-edge sites that are actually facet sites but are close to the edges: (1) CO₂RR is active at the near-edge sites on (111) facets, and (2) HER is active at the near-edge sites formed by two (111) and (100) facets. This led the octahedral AuNP, which is enclosed only by (111) facets without (100) facets, to exhibit not only the largest CO₂RR activity (i.e., high activity) but also the smallest HER activity (i.e., high selectivity).

We believe that our CE-*np* method, which can be generally employed for various nanocatalytic problems, provides an accurate and efficient route to investigate the catalytic activity of NPs with realistic sizes, particularly when the adsorbate binding energies barely correlate with the local coordinating geometry, such as the CN. Furthermore, our CE-*np* simulation results on the CO₂RR bring new insight into the active site of AuNPs, which can be utilized to design highly efficient and selective NP-based CO₂RR catalysts.

■ ASSOCIATED CONTENT

Supporting Information

The Supporting Information is available free of charge on the ACS Publications website at DOI: 10.1021/acs.jpcc.8b02886.

Atomic structures of AuNPs; DFT optimized structures of AuNPs with adsorbates; convergence behaviors during GA optimization; final sets of ECIs; correlations between DFT calculated binding energies and CNs; detailed procedures for estimating free energy quantities; comparisons of simulated current density and experimental data; relative ratio of (111) and (100) facets of AuNPs; and DFT calculated H, COOH, and CO binding energies (PDF)

■ AUTHOR INFORMATION

Corresponding Author

*E-mail: linus16@kaist.ac.kr.

ORCID

Hyung-Kyu Lim: 0000-0002-2403-2766

Yun Jeong Hwang: 0000-0002-0980-1758

Byoung Koun Min: 0000-0001-5766-0251

Hyungjun Kim: 0000-0001-8261-9381

Notes

The authors declare no competing financial interest.

■ ACKNOWLEDGMENTS

This work was supported by the Creative Materials Discovery Program (grant 2017M3D1A1039378), Nanomaterial Technology Development Program (grant 2016M3A7B4025414),

and Technology Development Program to Solve Climate Changes (grant 2015M1A2A2056561) through the National Research Foundation of Korea (NRF).

■ REFERENCES

- (1) Zhao, P.; Li, N.; Astruc, D. State of the Art in Gold Nanoparticle Synthesis. *Coord. Chem. Rev.* **2013**, *257*, 638–665.
- (2) Burda, C.; Chen, X.; Narayanan, R.; El-Sayed, M. A. Chemistry and Properties of Nanocrystals of Different Shapes. *Chem. Rev.* **2005**, *105*, 1025–1102.
- (3) Xia, Y.; Xiong, Y.; Lim, B.; Skrabalak, S. E. Shape-Controlled Synthesis of Metal Nanocrystals: Simple Chemistry Meets Complex Physics? *Angew. Chem., Int. Ed.* **2009**, *48*, 60–103.
- (4) Somorjai, G. A.; Frei, H.; Park, J. Y. Advancing the Frontiers in Nanocatalysis, Biointerfaces, and Renewable Energy Conversion by Innovations of Surface Techniques. *J. Am. Chem. Soc.* **2009**, *131*, 16589–16605.
- (5) Tian, N.; Zhou, Z.-Y.; Sun, S.-G.; Ding, Y.; Wang, Z. L. Synthesis of Tetrahedral Platinum Nanocrystals with High-Index Facets and High Electro-Oxidation Activity. *Science* **2007**, *316*, 732–735.
- (6) Zhou, Z.-Y.; Tian, N.; Li, J.-T.; Broadwell, I.; Sun, S.-G. Nanomaterials of High Surface Energy with Exceptional Properties in Catalysis and Energy Storage. *Chem. Soc. Rev.* **2011**, *40*, 4167–4185.
- (7) Kelly, K. L.; Coronado, E.; Zhao, L. L.; Schatz, G. C. The Optical Properties of Metal Nanoparticles: The Influence of Size, Shape, and Dielectric Environment. *J. Phys. Chem. B* **2003**, *107*, 668–677.
- (8) Rycenga, M.; Cobley, C. M.; Zeng, J.; Li, W.; Moran, C. H.; Zhang, Q.; Qin, D.; Xia, Y. Controlling the Synthesis and Assembly of Silver Nanostructures for Plasmonic Applications. *Chem. Rev.* **2011**, *111*, 3669–3712.
- (9) Bell, A. T. The Impact of Nanoscience on Heterogeneous Catalysis. *Science* **2003**, *299*, 1688–1691.
- (10) Norskov, J. K.; Abild-Pedersen, F.; Studt, F.; Bligaard, T. Density Functional Theory in Surface Chemistry and Catalysis. *Proc. Natl. Acad. Sci. U. S. A.* **2011**, *108*, 937–943.
- (11) Wang, L.-L.; Tan, T. L.; Johnson, D. D. Nanoalloy Composition-Temperature Phase Diagram for Catalyst Design: Case Study of Ag-Au. *Phys. Rev. B: Condens. Matter Mater. Phys.* **2012**, *86*, 035438.
- (12) Calle-Vallejo, F.; Tymoczko, J.; Colic, V.; Vu, Q. H.; Pohl, M. D.; Morgenstern, K.; Loffreda, D.; Sautet, P.; Schuhmann, W.; Bandarenka, A. S. Finding Optimal Surface Sites on Heterogeneous Catalysts by Counting Nearest Neighbors. *Science* **2015**, *350*, 185–189.
- (13) Zhu, W.; Michalsky, R.; Metin, O.; Lv, H.; Guo, S.; Wright, C. J.; Sun, X.; Peterson, A. A.; Sun, S. Monodisperse Au Nanoparticles for Selective Electrocatalytic Reduction of CO₂ to CO. *J. Am. Chem. Soc.* **2013**, *135*, 16833–16836.
- (14) Millstone, J. E.; Hurst, S. J.; Métraux, G. S.; Cutler, J. I.; Mirkin, C. A. Colloidal Gold and Silver Triangular Nanoprisms. *Small* **2009**, *5*, 646–664.
- (15) Wang, L.-L.; Tan, T. L.; Johnson, D. D. Configurational Thermodynamics of Alloyed Nanoparticles with Adsorbates. *Nano Lett.* **2014**, *14*, 7077–7084.
- (16) Cao, L.; Mueller, T. Rational Design of Pt₃Ni Surface Structures for the Oxygen Reduction Reaction. *J. Phys. Chem. C* **2015**, *119*, 17735–17747.
- (17) Tan, T. L.; Wang, L.-L.; Zhang, J.; Johnson, D. D.; Bai, K. Platinum Nanoparticle During Electrochemical Hydrogen Evolution: Adsorbate Distribution, Active Reaction Species, and Size Effect. *ACS Catal.* **2015**, *5*, 2376–2383.
- (18) Schmidt, D. J.; Chen, W.; Wolverton, C.; Schneider, W. F. Performance of Cluster Expansions of Coverage-Dependent Adsorption of Atomic Oxygen on Pt(111). *J. Chem. Theory Comput.* **2012**, *8*, 264–273.
- (19) Abrikosov, I. A.; Ruban, A. V.; Skriver, H. L.; Johansson, B. Calculated Orientation Dependence of Surface Segregations in

Pt50ni50. *Phys. Rev. B: Condens. Matter Mater. Phys.* **1994**, *50*, 2039–2042.

(20) Abrikosov, I. A.; Kissavos, A. E.; Liot, F.; Alling, B.; Simak, S. I.; Peil, O.; Ruban, A. V. Competition between Magnetic Structures in the Fe Rich Fcc FeNi Alloys. *Phys. Rev. B: Condens. Matter Mater. Phys.* **2007**, *76*, 014434.

(21) Sluiter, M. H. F.; Watanabe, Y.; de Fontaine, D.; Kawazoe, Y. First-Principles Calculation of the Pressure Dependence of Phase Equilibria in the Al-Li System. *Phys. Rev. B: Condens. Matter Mater. Phys.* **1996**, *53*, 6137–6151.

(22) van de Walle, A.; Ceder, G. Automating First-Principles Phase Diagram Calculations. *J. Phase Equilib.* **2002**, *23*, 348–359.

(23) Hart, G. L. W.; Blum, V.; Walorski, M. J.; Zunger, A. Evolutionary Approach for Determining First-Principles Hamiltonians. *Nat. Mater.* **2005**, *4*, 391–394.

(24) Ordejón, P.; Artacho, E.; Soler, J. M. Self-Consistent Order-N Density-Functional Calculations for Very Large Systems. *Phys. Rev. B: Condens. Matter Mater. Phys.* **1996**, *53*, R10441–R10444.

(25) Soler, J. M.; Artacho, E.; Gale, J. D.; García, A.; Junquera, J.; Ordejón, P.; Sánchez-Portal, D. The Siesta Method for Ab Initio Order-N Materials Simulation. *J. Phys.: Condens. Matter* **2002**, *14*, 2745–2779.

(26) Perdew, J. P.; Burke, K.; Ernzerhof, M. Generalized Gradient Approximation Made Simple. *Phys. Rev. Lett.* **1996**, *77*, 3865–3868.

(27) Junquera, J.; Paz, O.; Sánchez-Portal, D.; Artacho, E. Numerical Atomic Orbitals for Linear-Scaling Calculations. *Phys. Rev. B: Condens. Matter Mater. Phys.* **2001**, *64*, 235111.

(28) Blöchl, P. E. Projector Augmented-Wave Method. *Phys. Rev. B: Condens. Matter Mater. Phys.* **1994**, *50*, 17953–17979.

(29) Kim, C.; Eom, T.; Jee, M. S.; Jung, H.; Kim, H.; Min, B. K.; Hwang, Y. J. Insight into Electrochemical CO₂ Reduction on Surface-Molecule Mediated Ag Nanoparticles. *ACS Catal.* **2017**, *7*, 779–785.

(30) Kim, C.; Jeon, H. S.; Eom, T.; Jee, M. S.; Kim, H.; Friend, C. M.; Min, B. K.; Hwang, Y. J. Achieving Selective and Efficient Electrocatalytic Activity for CO₂ Reduction Using Immobilized Silver Nanoparticles. *J. Am. Chem. Soc.* **2015**, *137*, 13844–13850.

(31) Kim, K.-S.; Kim, W. J.; Lim, H.-K.; Lee, E. K.; Kim, H. Tuned Chemical Bonding Ability of Au at Grain Boundaries for Enhanced Electrochemical CO₂ Reduction. *ACS Catal.* **2016**, *6*, 4443–4448.

(32) Koh, J. H.; Won, D. H.; Eom, T.; Kim, N.-K.; Jung, K. D.; Kim, H.; Hwang, Y. J.; Min, B. K. Facile CO₂ Electro-Reduction to Formate Via Oxygen Bidentate Intermediate Stabilized by High-Index Planes of Bi Dendrite Catalyst. *ACS Catal.* **2017**, *7*, 5071–5077.

(33) Won, D. H.; Shin, H.; Koh, J.; Chung, J.; Lee, H. S.; Kim, H.; Woo, S. I. Highly Efficient, Selective, and Stable CO₂ Electroreduction on a Hexagonal Zn Catalyst. *Angew. Chem., Int. Ed.* **2016**, *55*, 9297–9300.

(34) Lu, Q.; Rosen, J.; Jiao, F. Nanostructured Metallic Electrocatalysts for Carbon Dioxide Reduction. *Chemcatchem* **2015**, *7*, 38–47.

(35) Mistry, H.; Reske, R.; Zeng, Z.; Zhao, Z.-J.; Greeley, J.; Strasser, P.; Cuenya, B. R. Exceptional Size-Dependent Activity Enhancement in the Electroreduction of CO₂ over Au Nanoparticles. *J. Am. Chem. Soc.* **2014**, *136*, 16473–16476.

(36) Reske, R.; Mistry, H.; Behafarid, F.; Cuenya, B. R.; Strasser, P. Particle Size Effects in the Catalytic Electroreduction of CO₂ on Cu Nanoparticles. *J. Am. Chem. Soc.* **2014**, *136*, 6978–6986.

(37) Sen, S.; Liu, D.; Palmore, G. T. R. Electrochemical Reduction of CO₂ at Copper Nanofoams. *ACS Catal.* **2014**, *4*, 3091–3095.

(38) Hansen, H. A.; Varley, J. B.; Peterson, A. A.; Nørskov, J. K. Understanding Trends in the Electrocatalytic Activity of Metals and Enzymes for CO₂ Reduction to CO. *J. Phys. Chem. Lett.* **2013**, *4*, 388–392.

(39) Peterson, A. A.; Abild-Pedersen, F.; Studt, F.; Rossmeisl, J.; Nørskov, J. K. How Copper Catalyzes the Electroreduction of Carbon Dioxide into Hydrocarbon Fuels. *Energy Environ. Sci.* **2010**, *3*, 1311–1315.

(40) Peterson, A. A.; Nørskov, J. K. Activity Descriptors for CO₂ Electroreduction to Methane on Transition-Metal Catalysts. *J. Phys. Chem. Lett.* **2012**, *3*, 251–258.

(41) Ferrin, P.; Kandoi, S.; Nilekar, A. U.; Mavrikakis, M. Hydrogen Adsorption, Absorption and Diffusion on and in Transition Metal Surfaces: A Dft Study. *Surf. Sci.* **2012**, *606*, 679–689.

(42) Lim, H.-K.; Shin, H.; Goddard, W. A.; Hwang, Y. J.; Min, B. K.; Kim, H. Embedding Covalency into Metal Catalysts for Efficient Electrochemical Conversion of CO₂. *J. Am. Chem. Soc.* **2014**, *136*, 11355–11361.

(43) Shin, H.; Ha, Y.; Kim, H. 2D Covalent Metals: A New Materials Domain of Electrochemical CO₂ Conversion with Broken Scaling Relationship. *J. Phys. Chem. Lett.* **2016**, *7*, 4124–4129.

(44) Nørskov, J. K.; Rossmeisl, J.; Logadottir, A.; Lindqvist, L.; Kitchin, J. R.; Bligaard, T.; Jónsson, H. Origin of the Overpotential for Oxygen Reduction at a Fuel-Cell Cathode. *J. Phys. Chem. B* **2004**, *108*, 17886–17892.

(45) Tritsarlis, G. A.; Greeley, J.; Rossmeisl, J.; Nørskov, J. K. Atomic-Scale Modeling of Particle Size Effects for the Oxygen Reduction Reaction on Pt. *Catal. Lett.* **2011**, *141*, 909–913.

(46) Zhu, W.; Zhang, Y.-J.; Zhang, H.; Lv, H.; Li, Q.; Michalsky, R.; Peterson, A. A.; Sun, S. Active and Selective Conversion of CO₂ to CO on Ultrathin Au Nanowires. *J. Am. Chem. Soc.* **2014**, *136*, 16132–16135.

(47) Back, S.; Yeom, M. S.; Jung, Y. Active Sites of Au and Ag Nanoparticle Catalysts for CO₂ Electroreduction to Co. *ACS Catal.* **2015**, *5*, 5089–5096.